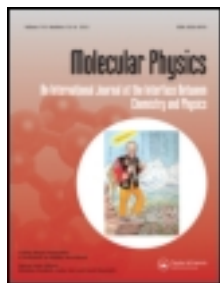


This article was downloaded by: [USC University of Southern California]

On: 11 October 2012, At: 17:42

Publisher: Taylor & Francis

Informa Ltd Registered in England and Wales Registered Number: 1072954 Registered office: Mortimer House, 37-41 Mortimer Street, London W1T 3JH, UK



Molecular Physics: An International Journal at the Interface Between Chemistry and Physics

Publication details, including instructions for authors and subscription information:

<http://www.tandfonline.com/loi/tmph20>

Electronic structure of tris(2-phenylpyridine)iridium: electronically excited and ionized states

J. Fine^a, K. Diri^a, A.I. Krylov^a, C. Nemirow^a, Z. Lu^a & C. Wittig^a

^a Department of Chemistry, University of Southern California, Los Angeles, CA 90089, USA

Accepted author version posted online: 27 Apr 2012. Version of record first published: 11 May 2012.

To cite this article: J. Fine, K. Diri, A.I. Krylov, C. Nemirow, Z. Lu & C. Wittig (2012): Electronic structure of tris(2-phenylpyridine)iridium: electronically excited and ionized states, *Molecular Physics: An International Journal at the Interface Between Chemistry and Physics*, 110:15-16, 1849-1862

To link to this article: <http://dx.doi.org/10.1080/00268976.2012.685899>

PLEASE SCROLL DOWN FOR ARTICLE

Full terms and conditions of use: <http://www.tandfonline.com/page/terms-and-conditions>

This article may be used for research, teaching, and private study purposes. Any substantial or systematic reproduction, redistribution, reselling, loan, sub-licensing, systematic supply, or distribution in any form to anyone is expressly forbidden.

The publisher does not give any warranty express or implied or make any representation that the contents will be complete or accurate or up to date. The accuracy of any instructions, formulae, and drug doses should be independently verified with primary sources. The publisher shall not be liable for any loss, actions, claims, proceedings, demand, or costs or damages whatsoever or howsoever caused arising directly or indirectly in connection with or arising out of the use of this material.

INVITED ARTICLE

Electronic structure of tris(2-phenylpyridine)iridium: electronically excited and ionized states

J. Fine, K. Dirí, A.I. Krylov*, C. Nemirow, Z. Lu and C. Wittig*

Department of Chemistry, University of Southern California, Los Angeles, CA 90089, USA

(Received 20 February 2012; final version received 28 March 2012)

A computational study of tris(2-phenylpyridine)iridium, Ir(ppy)₃, is presented. The perspective is that of using organo-transition-metal complexes as phosphorescent species in light-emitting diodes (OLED's). Quantum yields approaching 100% are possible through a triplet harvesting mechanism. Complexes such as Ir(ppy)₃ are amenable to exacting experimental and theoretical studies: small enough to accommodate rigor, yet large enough to support bulk phenomena in a range of host materials. The *facial* and *meridional* isomers differ by ~220 meV, with *fac*-Ir(ppy)₃ having the lower energy. Because *fac*-Ir(ppy)₃ dominates in most environments, focus is on this species. Time-dependent density functional theory using long-range-corrected functionals (BNL and ω B97X) is used to calculate excited states of Ir(ppy)₃ and a few low energy states of Ir(ppy)₃⁺. The calculated T₁–S₀ energy gap (2.30 eV) is in reasonable agreement with the experimental value of 2.44 eV. Only a few percent of singlet character in T₁ is needed to explain so short a phosphorescence lifetime as 200 ns, because of the large ¹LC ← S₀ and ¹MLCT ← S₀ absorption cross-sections. Equilibrium geometries are calculated for S₀, T₁, and the lowest cation state (D₀), and several ionization energies are obtained: adiabatic (5.86 eV); vertical from the S₀ equilibrium geometry (5.88 eV); and vertical ionization of T₁ at its equilibrium geometry (5.87 eV). These agree with a calculation by Hay (5.94 eV), and with the conservative experimental upper bound of 6.4 eV. Molecular orbitals provide qualitative explanations. A calculated UV absorption spectrum, in which transitions are vertical from the S₀ equilibrium geometry, agrees with the room temperature experimental spectrum. This is consistent with Franck–Condon factors dominated by $\Delta v_i = 0$, as expected given the delocalized nature of the orbitals. Ir(ppy)₃ vibrational frequencies were calculated and used to estimate the probability density $P(E_{vib})$ for 500 K, i.e. the temperature at which the experiments were carried out. In combination with the vibrational energy imparted through ¹LC ← S₀ photoexcitation, it is seen that a large amount of vibrational energy appears in Ir(ppy)₃⁺ without causing its fragmentation. Specifically, for $h\nu - E_{T_1} = 15,000 \text{ cm}^{-1}$, the probability density for *total* vibrational energy peaks at ~31,000 cm⁻¹ with a 7800 cm⁻¹ width.

Keywords: ionization; TDDFT; long-range-corrected functionals; internal conversion; intersystem crossing; phosphorescence; iridium complexes; spin-orbit coupling; OLED

1. Introduction

The use of organo-transition-metal complexes as phosphorescent species in light-emitting diodes (OLEDs) enables quantum yields approaching 100% to be achieved through a mechanism referred to as triplet harvesting [1–5]. In triplet harvesting, spin-orbit coupling (SOC) enables electronic excitation that originates with electron-hole recombination (i.e. both singlet and triplet excitons) to relax non-radiatively to the lowest triplet, T₁. In turn, T₁ undergoes T₁ → S₀ phosphorescence with near 100% quantum efficiency. This high quantum efficiency is also a consequence of SOC [1–7]. Namely, SOC results in short enough T₁ → S₀ phosphorescence lifetimes to render T₁ non-radiative decay ineffective.

Such OLEDs offer great advantage over purely organic counterparts, whose maximum quantum yield

is 25%, i.e. the singlet exciton fraction that results from electron-hole recombination with a statistical distribution of spin states [1–7]. In other words, phosphorescence is not a viable means of obtaining photons in organics because SOC is negligible, and consequently triplet excitation is lost rather than harvested.

As the light-emitting ingredient in OLED devices, organo-transition-metal complexes play a central role in the rapidly evolving research area of display technologies. With billions of euros at stake, motivation from the high-tech commercial sector has never been higher. At the same time, these complexes are amenable to exacting and symbiotic experimental and theoretical studies. To wit, they are small enough to accommodate rigor, yet large enough to support bulk phenomena in a range of host materials. The OLED systems that are based on organo-transition-metal

*Corresponding authors. Email: krylov@usc.edu; wittig@usc.edu

complexes are both technologically important and scientifically interesting, and their study benefits from, and is well suited to, mix-and-match interdisciplinary approaches.

An overview of OLEDs as they relate to the experiments and calculations carried out in our groups is presented in the Introduction of the accompanying (i.e. preceding) paper, hereafter referred to as Paper I [8]. The reader is encouraged to read, at the very least, the Introduction in Paper I, as none of this is repeated below. In Paper I, several experimental results are presented and discussed, and possible interpretations are considered, in some cases enlisting comparisons with the calculated results presented herein.

In the present paper, tris(2-phenylpyridine)iridium, hereafter referred to as Ir(ppy)₃, is examined using time dependent density functional theory; details concerning its use in the present study are given in the next section. The goal is to obtain qualitative — and to the extent possible quantitative — understanding of low-lying singlets and triplets of Ir(ppy)₃, and of low-lying doublets of the cation Ir(ppy)₃⁺. This includes structural properties, spectral properties, molecular orbital (MO) descriptions, and ionization energies. The latter is germane to OLED devices because the ionization energies and electron affinities (commonly referred to as the HOMO and LUMO energies, respectively) of the light-emitting molecules in the active layer need to be matched to the energy levels of the electrodes.

There are two low-energy Ir(ppy)₃ isomers: *facial* and *meridional*, hereafter referred to as *fac*-Ir(ppy)₃ and *mer*-Ir(ppy)₃, respectively. As discussed later, the energy difference between them is $\sim 1800\text{ cm}^{-1}$ ($\sim 220\text{ meV}$) [9,10], with the *fac* isomer the more stable of the two. This is sufficient to rule out the participation of *mer*-Ir(ppy)₃ in most environments. Consequently, though some calculations were carried out on the *mer*-Ir(ppy)₃ system, the main focus of the present study is *fac*-Ir(ppy)₃.

The work reported herein builds on and complements earlier theoretical studies [9–13], and it assists in the interpretation of experimental results [14–17], including, but not limited to, those presented in Paper I. Organization of the paper is as follows. Computational strategies and procedures are presented and discussed in Section 2. This is followed (in Section 3) by the results, and discussions of their relevance to experimental data and practical applications. These results include: equilibrium structures; vertical and adiabatic ionization energies; MO descriptions obtained at the equilibrium structures of the ground state (S_0), lowest triplet (T_1), and lowest ionized state (D_0); the ultraviolet absorption spectrum; comparison to experimental T_1 phosphorescence

parameters (T_1 – S_0 energy gap, spontaneous emission lifetimes, and Franck–Condon factors); and an interesting point regarding the probability density for T_1 vibrational energy following photoexcitation of gaseous Ir(ppy)₃ at 500 K, i.e. the temperature at which the experiments presented in Paper I were carried out [8]. The paper concludes with a brief summary.

2. Computational details

Two long-range-corrected (LRC) functionals were used: ω B97X and BNL [18–21]. Each treats the long-range Coulomb interaction exactly (i.e. 100% Hartree–Fock exchange), thus ensuring proper asymptotic behavior and mitigating the notorious self-interaction errors [22]. Specifically, these functionals reduce the unphysical charge delocalization that is often observed when using standard functionals such as B3LYP. They also eliminate contamination of time dependent density functional theory (TDDFT) results by an artificially low-lying Rydberg manifold that converges to the Koopmans ionization energy (IE), which is underestimated when using non-LRC functionals.

Our choice is based on the following considerations. The ω B97X functional has been carefully parameterized and benchmarked [18,19]. It consistently gives more accurate structures and standard thermochemical quantities than, for example, B3LYP. Thus, structures calculated using ω B97X are taken as our best estimates. The BNL functional has been developed for excited states. Its range-separation parameter ω is system-dependent, and it is chosen such that the Koopmans IE is equal to the vertical ionization energy (VIE), a condition that should be satisfied for the exact exchange-correlation functional. BNL performs well for excited and ionized states, including ionization from lower orbitals [20,21]. Thus, we expect its IE's and excited state energies to be of higher quality than the ω B97X ones.

Structures of *fac*-Ir(ppy)₃ and *mer*-Ir(ppy)₃ in the S_0 , T_1 , and D_0 states were optimized using the ω B97X functional [18,19]. For the iridium atom, the lanl2dz basis was employed, whereas 6–311G++(d,p) was used for all other atoms [23,24]. The range-separation parameter ω in the BNL functional was optimized such that the VIE that was computed using the energy differences method (Δ SCF) matched the HOMO energy (Koopmans IE) at the S_0 equilibrium geometry. This yielded $\omega = 0.17 a_0^{-1}$ [18]. The default ω value for BNL is $0.50 a_0^{-1}$, and the ω value in ω B97X is fixed at $0.3 a_0^{-1}$ [20,25,26] (as mentioned above, BNL ω values are system specific).

The IEs were calculated using Koopmans theorem, which has been shown to yield accurate results for the BNL functional, owing to its LRC character and a system-specific choice of ω . Moreover, the BNL orbitals provide a reasonable representation of the ionized state, which is not the case for B3LYP. The shape of the hole in the ionized state can be verified by calculating the spin density: $\rho(\alpha) - \rho(\beta)$, for each MO. This accounts for non-Koopmans character, i.e. orbital relaxation. This analysis was carried out for D_0 at selected geometries.

Excited states were calculated at the S_0 and T_1 geometries using TDDFT with ω B97X and BNL functionals and lan12dz and 6-311+G(d,p) bases. At the S_0 geometry, 50 singlet and 50 triplet states were calculated using ω B97X, spanning the energy range 2.86–6.31 eV. With BNL at the S_0 geometry, 130 singlets and 130 triplets were calculated, spanning the energy range 2.56–5.66 eV. With BNL at the T_1 geometry, only the 10 lowest singlet and 10 lowest triplet states were calculated.

The TDDFT excited state energies and oscillator strengths were used to calculate absorption spectra. Gaussian shaped spectral densities, $g_i(E)$, were assigned to each of the transitions in a given theoretical ‘stick spectrum’. Specifically, the absorption spectrum was simulated as a sum of Gaussian spectral densities, $g_i(E)$, each having the same width parameter σ :

$$g_i(E) = f_i(2\pi\sigma^2)^{-1/2} \exp\left(-\frac{(E - E_i)^2}{2\sigma^2}\right) \quad (1)$$

The factor f_i is the oscillator strength of the electric dipole transition from the S_0 ground state to the i th electronic state. Each Gaussian spectral density is centred at its excited state energy, E_i . The width parameter σ is related to the full width at half maximum (FWHM) of the Gaussian distribution

according to: $\text{FWHM} = 2(2 \ln 2)^{1/2} \sigma = 2.35 \sigma$. All calculations were carried out using the QChem electronic structure package [27].

3. Results and discussion

In this section, the strategies and procedures described in Section 2 are applied to calculations of properties of $\text{Ir}(\text{ppy})_3$ and $\text{Ir}(\text{ppy})_3^+$. A number of technical details and data sets that are omitted from the text for the sake of brevity are included as electronically available Supplementary Material (SM). Reference to the SM is made whenever appropriate. Energies and frequencies are given in wavenumbers (cm^{-1}), with eV counterparts in parentheses. On occasion, kcal mol^{-1} is used, i.e. when comparing to literature values given in these units.

3.1. Equilibrium structures

The ground electronic state structures of *fac*- $\text{Ir}(\text{ppy})_3$ and *mer*- $\text{Ir}(\text{ppy})_3$ are indicated in Figure 1. As discussed below, their energies differ by $\sim 1800 \text{ cm}^{-1}$ ($\sim 220 \text{ meV}$) with *fac*- $\text{Ir}(\text{ppy})_3$ the more stable of the two. Table 1 lists selected bond lengths for *fac*- $\text{Ir}(\text{ppy})_3$ at its S_0 and T_1 equilibrium geometries, and for $\text{Ir}(\text{ppy})_3^+$ at the equilibrium geometry of the lowest energy cation state, D_0 . Table 2 lists selected bond lengths for the S_0 and D_0 equilibrium geometries of *mer*- $\text{Ir}(\text{ppy})_3$. The z -matrices and relevant energies are provided in the SM.

Referring to Table 1, the equilibrium bond lengths of ground state *fac*- $\text{Ir}(\text{ppy})_3$ are compared with results of x -ray diffraction measurements of *fac*- $\text{Ir}(\text{ppy})_3$ [28,29] and of its tolylpyridine analogue *fac*- $\text{Ir}(\text{tpy})_3$ [30], as well as with previous theoretical estimates [10,11]. The T_1 equilibrium structure is compared to

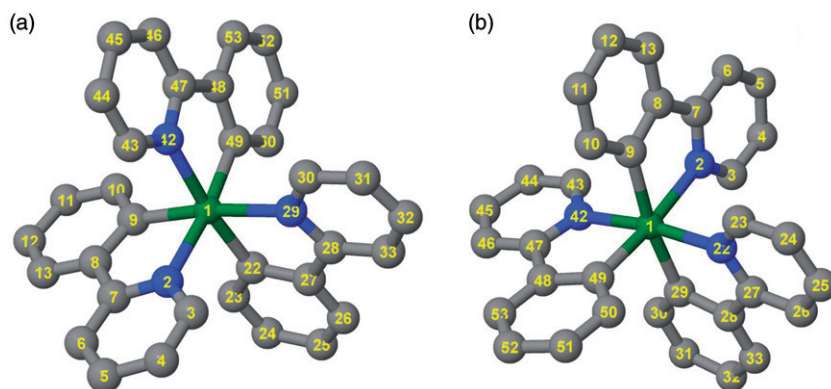


Figure 1. Ground electronic state structures and atom numbering for (a) *fac*- $\text{Ir}(\text{ppy})_3$ and (b) *mer*- $\text{Ir}(\text{ppy})_3$. H atoms are omitted. Color scheme: green = Ir; blue = N; gray = C. Tables 1 and 2 list geometrical parameters.

Table 1. Bond lengths (Å) for S₀, T₁, and D₀ states of Ir(ppy)₃.

	S ₀ (theory)			S ₀ (expt)			T ₁ (theory)		D ₀ (theory)
	(a)	(b)	(c)	(d)	(e)	(f)	(a)	(b)	(a)
Ir–N ₂	2.168	2.153	2.167	2.088	2.071	2.132	2.196	2.176	2.148
Ir–N ₂₉	2.169	2.154	2.167	2.088	2.071	2.132	2.175	2.169	2.184
Ir–N ₄₂	2.165	2.151	2.167	2.088	2.071	2.132	2.139	2.116	2.213
Ir–C ₉	2.025	2.035	2.035	2.006	2.060	2.024	2.025	2.030	2.028
Ir–C ₂₂	2.023	2.035	2.035	2.006	2.060	2.024	2.036	2.048	1.975
Ir–C ₄₉	2.022	2.035	2.035	2.006	2.060	2.024	1.961	2.000	2.035
N ₂ –C ₃ ,N ₂₉ –C ₃₀	1.34	1.36	–	1.345	1.361	1.331	1.34	1.36	1.34, 1.34
N ₄₂ –C ₄₃	1.34	1.36	–	1.345	1.361	1.331	1.33	1.36	1.34
N ₂ –C ₇ ,N ₂₉ –C ₂₈	1.35	1.38	–	1.358	1.385	1.371	1.35	1.38	1.355, 1.35
N ₄₂ –C ₄₇	1.35	1.38	–	1.358	1.385	1.371	1.40	1.439	1.35
C ₉ –C ₁₀ ,C ₂₂ –C ₂₃	1.405	1.42	–	1.405	1.374	1.401	1.40	1.42	1.395, 1.41
C ₄₉ –C ₅₀	1.405	1.42	–	1.405	1.374	1.401	1.41	1.42	1.40
C ₈ –C ₉ ,C ₂₂ –C ₂₇	1.415	1.44	–	1.423	1.396	1.409	1.41	1.43	1.41, 1.407
C ₄₈ –C ₄₉	1.415	1.436	–	1.423	1.396	1.409	1.49	1.485	1.426
C ₇ –C ₈ ,C ₂₇ –C ₂₈	1.47	1.47	–	–	–	1.487	1.47	1.47	1.47, 1.476
C ₄₇ –C ₄₈	1.47	1.467	–	–	–	1.487	1.40	1.419	1.473

(a) current work, (b) [11], (c) [10], (d) [28], (e) [29], (f) [30].

Table 2. Bond lengths (Å) for S₀ and D₀ *mer*-Ir(ppy)₃.

	S ₀ (theory)	S ₀ (expt)	D ₀ (theory)
	(a)	(b)	(a)
Ir–N ₂	2.193	2.151	2.275
Ir–N ₂₂	2.079	2.044	2.083
Ir–N ₄₂	2.068	2.065	2.077
Ir–C ₉	2.101	2.086	2.094
Ir–C ₂₉	2.078	2.076	2.070
Ir–C ₄₉	2.006	2.020	1.973
N ₂ –C ₃ ,N ₂₂ –C ₂₃	1.34, 1.34		1.34, 1.34
N ₄₂ –C ₄₃	1.34		1.34
N ₂ –C ₇ ,N ₂₂ –C ₂₇	1.35, 1.36		1.35, 1.354
N ₄₂ –C ₄₇	1.355		1.353
C ₉ –C ₁₀ ,C ₂₉ –C ₃₀	1.404, 1.40		1.40, 1.394
C ₄₉ –C ₅₀	1.404		1.404
C ₈ –C ₉ ,C ₂₈ –C ₂₉	1.414, 1.41		1.40, 1.406
C ₄₈ –C ₄₉	1.413		1.42
C ₇ –C ₈ ,C ₂₇ –C ₂₈	1.48, 1.47		1.47, 1.47
C ₄₇ –C ₄₈	1.464		1.47

(a) current work, (b) [17].

the calculations of Jansson *et al.* [11]. Referring to Table 2, the calculated *mer*-Ir(ppy)₃ structure is compared with the crystallographic structure of its tolylpyridine analog: *mer*-Ir(tpy)₃ [17].

Variations in the experimentally determined bond lengths arise, at least in part, because of different experimental conditions. For example, the high pressure crystallographic structure reported by Breu *et al.* [29] showed that the *fac*-Ir(ppy)₃ crystal has a racemic

unit cell (three Δ and three Λ complexes in the P $\bar{3}$ point group). Thus, though isolated ground state *fac*-Ir(ppy)₃ molecules are of C₃ symmetry, they can develop different equilibrium bond lengths when exposed to local environments.

Table 1 includes entries from one of the three data sets reported in [29]. Specifically, the set chosen for comparison with our calculated values is the one that displays the *largest* differences with our values. Differences in bond lengths among the data sets reported in [29] are within 0.03 Å of one another. Differences between all reported experimental values are slightly larger, i.e. approximately 0.04 and 0.05 Å for Ir–N and Ir–C bond lengths, respectively, but less than 0.02 Å for all other bond lengths. All crystallographic structures are of similar quality, with a reported bond length uncertainty < 1%.

The *fac*-Ir(ppy)₃ ground state structure was optimized with no symmetry constraints. It deviates slightly from C₃ symmetry due to numerical thresholds used in optimization, and the inability of Cartesian integration grids to support groups like C₃. Our calculated structure is similar to the one reported by Jansson *et al.* [11], and it is in reasonable agreement with other theoretical values [10], despite the fact that they were obtained at a lower level of theory. The computed Ir–C and Ir–N bond lengths are closest to the experimental values reported in [30]. The deviations are 0.001 and 0.04 Å for Ir–C and Ir–N, respectively. The NC and CC bond lengths are within 0.01 Å of the values reported in [28], while deviations from the values reported in [29] are about 0.03 Å.

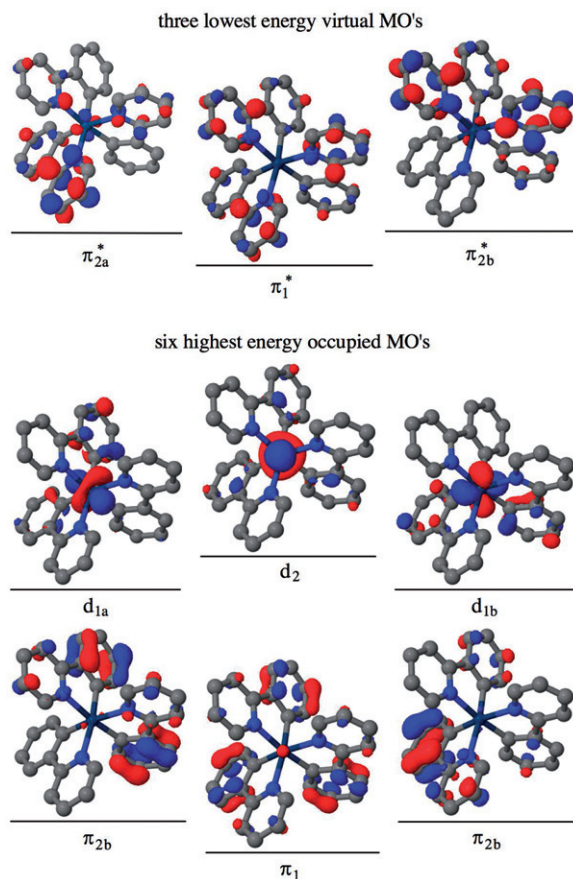


Figure 2. Six highest occupied MOs and three lowest virtual MOs for *fac*-Ir(ppy)₃ at S₀ geometry using BNL: Orbital labeling follows Hay [10]. Energies of occupied orbitals (Koopmans IE's) are given in Table 3.

Referring to Figure 2, π_{2a}^* and π_{2b}^* are components of a doubly degenerate *e* orbital. Consequently, T₁ and D₀ each exhibit Jahn-Teller distortion that breaks C₃ symmetry. In T₁, relative to the S₀ values, two ligands move away from the iridium atom and one is drawn closer to the iridium atom. Specifically, the closer ligand corresponds to Ir–C₄₉ and Ir–N₄₂ in our calculations (see Figure 1 for numbering of atoms). The D₀ structure follows a similar pattern. The Ir–C₂₂ and Ir–N₂ bonds contract, whereas the other metal-ligand bonds lengthen relative to their S₀ values. An interesting difference between T₁ and D₀ is that the contracted bonds in D₀ are not part of the same ligand. These structural changes are consistent with the MO shapes, as discussed later.

Calculations were also carried out for the *mer*-Ir(ppy)₃ isomer whose structure is indicated in Figure 1(b). The results are summarized in Table 2. When using ω B97X and BNL, the *mer* isomer is calculated to be less stable than the *fac* isomer by 280 and 220 meV (2270 and 1760 cm⁻¹, 6.5 and

5.0 kcal mol⁻¹), respectively. These values are total electronic energy differences, Δ SCF. This is consistent with previous theoretical [9,10] and experimental [17] results.

Despite the apparent similarity between the *fac* and *mer* isomers seen in Figure 1, bonding is different. In the *mer* isomer, the three nitrogen atoms lie in a plane that contains the iridium atom (with two nitrogen atoms lying on a straight N–Ir–N line), whereas in the *fac* isomer the nitrogen atoms form an equilateral triangle with the iridium atom out of the plane on the C₃ axis. This difference, in which the *mer* isomer is obtained from the *fac* isomer by rotating a single ligand 180° about its \angle C–Ir–N bisection line, places two phenyl groups, and consequently two pyridyl groups, *trans* to one another.

As shown in Table 2, and referring to the *mer* isomer indicated in Figure 1(b), its *trans* Ir–C bonds (i.e. Ir–C₉ and Ir–C₂₉) are longer than the Ir–C bonds in *fac*-Ir(ppy)₃, while the remaining *mer* Ir–C₄₉ bond length is nearly equal to the *fac* Ir–C bond length. Also note that the remaining Ir–C₄₉ bond has an environment that is similar to that of the *fac* Ir–C bonds, in the sense that it is perpendicular to two Ir–N bonds (i.e. Ir–N₂₄ and Ir–N₄₂). Thus, it is not surprising that their lengths are similar. On the other hand, the *trans* Ir–C bonds do not share the same environment as the Ir–C bonds in the *fac* isomer, in the sense that they are perpendicular to all three Ir–N bonds.

The extended Ir–C bond lengths are consistent with the weaker structural *trans*-effect, often called the *trans* influence [31,32], of a pyridyl group relative to a phenyl group. A similar analysis of the *mer* Ir–N bonds shows that the *trans* N–Ir–N bonds are noticeably shorter than in the *fac* isomer. This is again consistent with the weaker structural *trans*-effect of the pyridyl group. Our predicted *mer* structure is in reasonable agreement with the *x*-ray data for *mer*-Ir(tpy)₃, i.e. bond lengths are within 0.04 Å of the experimental values [17].

In making comparisons to the experimental work presented in Paper I, it is possible to rule out significant participation of the *mer*-Ir(ppy)₃ isomer. Specifically, the energy gap between the *fac* and *mer* isomers, say 220 meV (i.e. the BNL value), is large enough that at 500 K the *mer*-Ir(ppy)₃ population is only $\exp(-E_{mer}/kT) = \exp(-5.12) \approx 0.6\%$ of that of *fac*-Ir(ppy)₃. Thus, hereafter only the *fac*-Ir(ppy)₃ isomer will be considered.

3.2. Molecular orbitals

The molecular orbitals (MOs) of *fac*-Ir(ppy)₃ that are most relevant to the present study are shown in

Table 3. Koopmans IEs (eV) for the six highest energy occupied MO's of *fac*-Ir(ppy)₃.

MO	BNL	ω B97X
d ₂	-5.87	-7.42
d _{1a} , d _{1b}	-6.06	-7.49
π_{2a} , π_{2b}	-7.15	-8.45
π_1	-7.27	-8.59

Figure 2, and the orbital energies (Koopmans IEs) for the six highest energy occupied MOs are listed in Table 3. As mentioned earlier, the use of an LRC functional reduces artificial delocalization caused by self-interaction error. Consequently, the LRC functionals used here yield MOs that represent the character of the excited and ionized states better, for example, than does B3LYP. In addition, the Koopmans IEs with BNL are more reliable [33].

Referring to Figure 2, the three highest occupied molecular orbitals at the S₀ equilibrium geometry are of mixed 5d- π character. They are labelled: d_{1a}, d_{1b}, and d₂, and they will also be referred to as HOMO-1, HOMO-2, and HOMO, respectively. The d₂ HOMO is dominated by the iridium 5dz² orbital, but with a π contribution that arises almost entirely from the phenyl groups. The d_{1a} and d_{1b} orbitals, which are components of a doubly degenerate *e* orbital, consist of combinations of d-orbitals, with a somewhat larger contribution from the phenyl groups than in the case of d₂.

The three lowest energy MO's in Figure 2 are primarily of π character, with most of the electron density residing on the phenyl groups. They have less than 4% iridium character. The lowest energy virtual orbitals are primarily of π^* character in the pyridyl group. These lowest virtual orbitals are of *e* and *a* symmetries, with π_{2a}^* and π_{2b}^* being components of a doubly degenerate *e* orbital. From the Jahn-Teller theorem, single occupancy of *e* orbitals will lead to symmetry lowering in excited and ionized states. This is consistent with orbital localization in which the HOMO becomes asymmetrically distributed among the ligands. It is also consistent with the results reported by Jansson *et al.* [11].

This above picture is consistent qualitatively with previous findings [10–12]. However, relative to previous calculations, our orbitals are more localized, owing to the use of LRC functionals. This was confirmed by a shell population analysis of S₀ (details are given in the SM). Iridium comprised 58% of the HOMO character, but only 48% of the HOMO-1 and HOMO-2 character.

The shape of the hole in the cation has been verified by spin density calculations that account for non-Koopmans character, i.e. orbital relaxation. The spin density analysis is in qualitative agreement with a Koopmans description of the electron hole (Figure 3). A summary of Mulliken spin densities of the cation at S₀, T₁, and D₀ geometries is given in Table 4, and the HOMOs from which an electron is removed are shown in Figure 3. It is seen that structural relaxation causes the amount of iridium character in the electron hole to increase from 58% to 65%. The complete list of Mulliken spin densities for all three geometries is provided in the SM.

Referring to Figure 3(a) and Table 4, the HOMO at the S₀ geometry, and therefore the character of the cation hole of S₀, is the d₂ orbital indicated in Figure 2. (Note that the orbital shown in Figure 3(a) is identical to the d₂ orbital in Figure 2.) Therefore, the hole is symmetric with the iridium atom hosting most of the hole spin density. The remaining $\approx 35\%$ is distributed over the three phenyl groups. In each phenyl group (see Figure 4), carbons C1, C2, and C3 account for most of the spin density.

At the D₀ and T₁ equilibrium geometries, the HOMO differs considerably from that of the S₀ equilibrium geometry. First, the HOMO at the D₀ equilibrium geometry has a large percentage of its density on the phenyl group drawn closest to iridium. It resembles the d_{1a} orbital in Figure 2. Much of the hole spin density in the cation resides on the carbons C1, C2, and C3 indicated in Figure 4.

Now consider T₁ at its equilibrium geometry. The ligand closest to the iridium atom contains nearly all of the ligand portions of the HOMO and LUMO that describe T₁, as indicated in Figure 5. Note that the HOMO in Figure 5(d) is identical to the electron hole wave function (at the T₁ equilibrium geometry) in Figure 3(b). In contrast to the D₀ hole in Figure 3(c), the T₁ hole in Figure 3(b) has more amplitude over the pyridyl group of the closest ligand. The pyridyl atoms hosting most of the spin density are those labeled N42, C44, and C46 in Figure 1(a).

Furthermore, because the character of the HOMO changes from d₂ at the S₀ geometry to d_{1a} at the D₀ and T₁ geometries, the electronic character of the cation ground state changes upon these displacements. In other words, the d₂ and d_{1a}/d_{1b} orbitals (and consequently the respective diabatic states of the cation) change their relative order. This is not surprising in view of the small energy gap between them (0.19 eV) at the S₀ geometry.

The Koopmans IEs for the six highest-energy occupied MOs are listed in Table 3. Due to small deviations from C₃ symmetry, the energies of

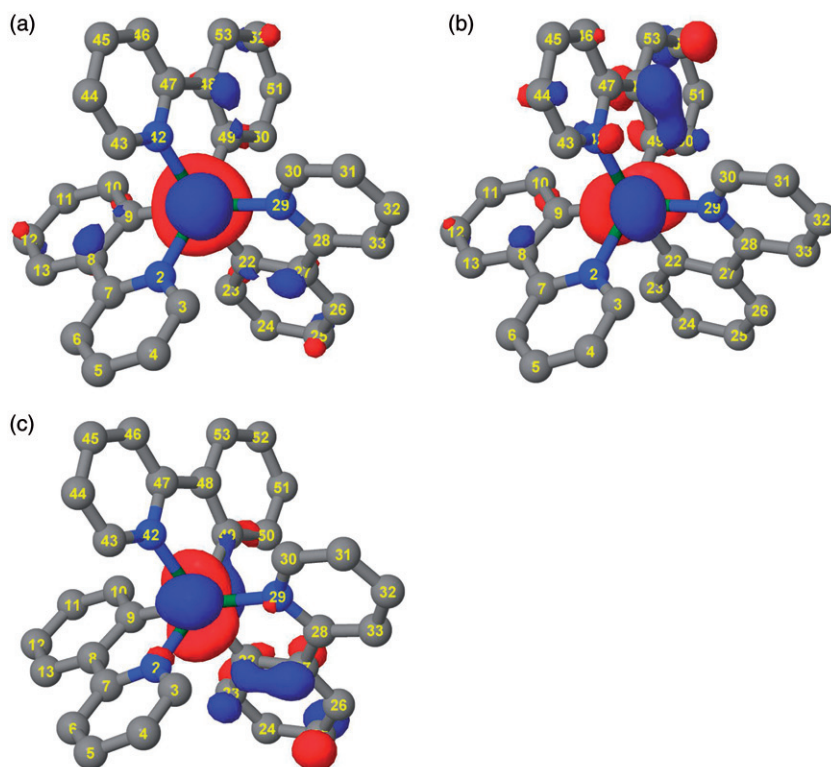


Figure 3. Shapes of the electron hole wave functions obtained from Koopmans analyses for cations at the (a) S_0 , (b) T_1 , and (c) D_0 equilibrium geometries.

Table 4. BNL percent spin density for *fac*-Ir(ppy)₃ at the S_0 , T_1 , and D_0 equilibrium geometries. For T_1 and D_0 , only the main contributions are listed.

	Mulliken spin density of hole			
	Ir	C ₁	C ₂	C ₃
S_0	67	~4 ^a	~4 ^a	~4 ^a
T_1	58	12	11	6
D_0	61	10	13	10

^aFor S_0 there are 3 identical sets of carbon atoms (C₁, C₂, C₃), so the listed percentages (~4) need to be multiplied by 3 to account for the 9 main participating carbon atoms.

degenerate e orbitals are slightly different (<0.01 eV), so we report the average of the two values. As seen in Table 3, the density of electronic states in the cation is rather high, i.e. there are 6 cation states in the range: 5.87–7.27 eV. The difference between the BNL and ω B97X values is due to different values of ω . Based on the previous benchmarks and reported VIE values, the BNL results are expected to be more reliable.

Adiabatic and vertical IEs calculated as a total energy difference are presented in Table 5 for S_0 and

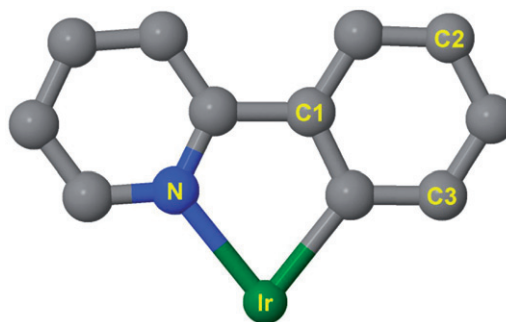


Figure 4. Ir(ppy) corresponding to Table 4: for the T_1 equilibrium geometry, C1, C2, and C3 correspond to carbons labeled 48, 52, and 50 in Figure 1(a) [see also Figure 3(b)]. For the D_0 equilibrium geometry C1, C2, and C3 correspond to carbons labelled 23, 25, and 27 in Figure 1(a) [see also Figure 3(c)].

T_1 geometries. The small difference between the BNL VIE and AIE values (≤ 0.02 eV) for S_0 and T_1 suggests that structural relaxation caused by the removal of a single electron is small, possibly because of the delocalized character of the orbitals. The use of ω B97X results in a larger difference between VIE and

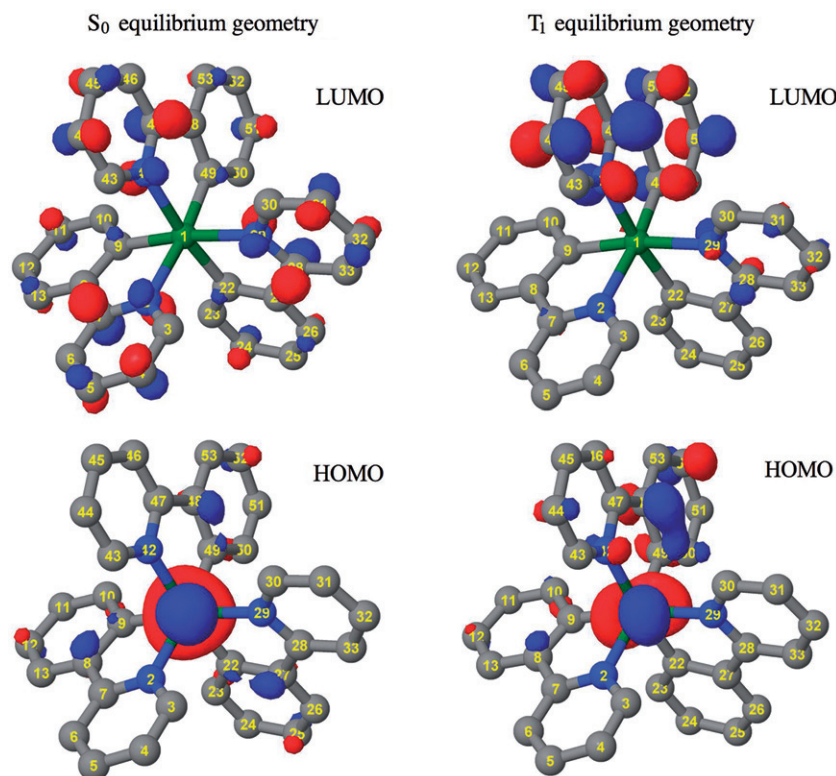


Figure 5. Orbitals giving rise to T_1 excitation (HOMO and LUMO of S_0): left and right columns correspond, respectively, to S_0 and T_1 equilibrium geometries.

Table 5. Vertical and adiabatic IEs (eV) for *fac*-Ir(ppy)₃ from S_0 and T_1 states at their equilibrium geometries.

	BNL		ω B97X	
	VIE	AIE	VIE	AIE
S_0	5.87	5.86	6.42	6.33
T_1	3.40	3.38	3.98	3.52

AIE than BNL for both S_0 and T_1 (0.09 eV for S_0 and 0.46 eV for T_1).

The only previously reported theoretical estimate of the VIE from S_0 is 5.94 eV [10], while the only previously reported experimental value is an indirect inference of 7.2 eV [16]. Our experimental study (Paper I) provides a conservative VIE upper bound of 6.4 eV [8]. Both BNL and ω B97X values (5.87 and 6.42 eV, respectively) agree with this experimentally derived upper bound. However, the BNL value is the more accurate estimate for the reasons given in Section 2.

3.3. Ultraviolet absorption spectrum

Figure 6 shows experimental and calculated ultraviolet absorption spectra. All excited state energies and

oscillator strengths were evaluated at the ground state equilibrium geometry. As discussed in Section 2, BNL gives the most reliable excited states. Therefore, it is the BNL spectrum that is compared to the experimental spectrum.

Although ω B97X yielded good values for ground state equilibrium structures (Figure 1, Tables 1 and 2), it is inferior insofar as excited states are concerned, e.g. see the comparison in the inset in Figure 6. The ω B97X spectrum was computed using the first 50 singlets, whereas for the BNL spectrum, 130 singlets were necessary to achieve convergence. Selected BNL excitation energies are given in Tables 6 and 7. A complete list of the calculated excited states and oscillator strengths that were used to construct the theoretical spectra is given in the SM.

Referring to Equation (1), a width parameter of $\sigma = 0.185$ eV (corresponding to Gaussian FWHM of 0.43 eV) was obtained from a least-squares fit of the BNL spectrum to the experimental spectrum. No attempt was made to calculate absolute intensities. Thus, the vertical axis in Figure 6 is not labelled. The BNL curve was scaled such that its maximum is the same height as the maximum of the experimental spectrum. These calculations do not include contributions from triplets due to SOC. The low-energy part of

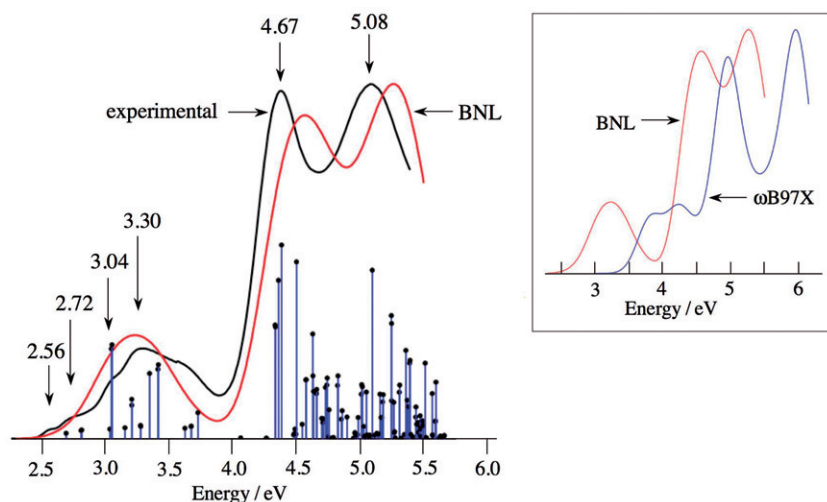


Figure 6. Ultraviolet absorption spectra of *fac*-Ir(ppy)₃. The calculated spectrum (red) was obtained from the stick spectrum by assigning to each stick a Gaussian FWHM of 0.43 eV. The experimental spectrum (black) was recorded at room temperature in dichloromethane. Peak and shoulder positions (vertical arrows) are in eV. All stick heights have been increased by the same constant factor for viewing convenience, and curve height has been adjusted such that the maximum absorptions are equal. The low-energy, low-intensity wing due to $T_1 \leftarrow S_0$ (2.56 eV) is absent in the calculated spectrum because SOC was not included. Inset: the BNL (red) and ω B97X (blue) spectra differ considerably, the latter being far out of registry with the experimental spectrum.

Table 6. Orbital character and leading amplitude for the four lowest energy triplet states at the S_0 and T_1 equilibrium geometries: Energies are relative to that of S_0 at its equilibrium geometry.

State	S_0 geometry			T_1 geometry		
	Energy	Leading character	Amplitude	Energy	Leading character	Amplitude
T_1	2.56	$d_2 \rightarrow \pi_1^*$	0.89	2.30	$d_2 \rightarrow \pi_1^*$	0.87
T_2	2.61	$d_2 \rightarrow \pi_{2a}^*$	0.59	2.74	$d_{1a} \rightarrow \pi_1^*$	0.71
		$d_2 \rightarrow \pi_{2b}^*$	-0.54			
T_3	2.62	$d_2 \rightarrow \pi_{2a}^*$	0.59	2.78	$d_2 \rightarrow \pi_{2b}^*$	0.47
		$d_2 \rightarrow \pi_{2b}^*$	0.53		$d_{1b} \rightarrow \pi_1^*$	0.46
T_4	2.83	$d_2 \rightarrow \pi_{2a}^*$	0.67	2.82	$d_2 \rightarrow \pi_{2b}^*$	-0.46

Table 7. Orbital character and leading amplitude for the three lowest energy singlet excited states at the S_0 and T_1 equilibrium geometries. Energies are relative to that of S_0 at its equilibrium geometry.

State	S_0 geometry			T_1 geometry		
	Energy	Character	Amplitude	Energy	Character	Amplitude
S_1	2.69	$d_2 \rightarrow \pi_1^*$	0.94	2.62	$d_2 \rightarrow \pi_1^*$	0.95
S_2	2.80	$d_2 \rightarrow \pi_{2a}^*$	0.90	2.91	$d_2 \rightarrow \pi_{2a}^*$	0.82
S_3	2.81	$d_{1b} \rightarrow \pi_{2a}^*$	0.90	2.96	$d_2 \rightarrow \pi_{2b}^*$	0.84

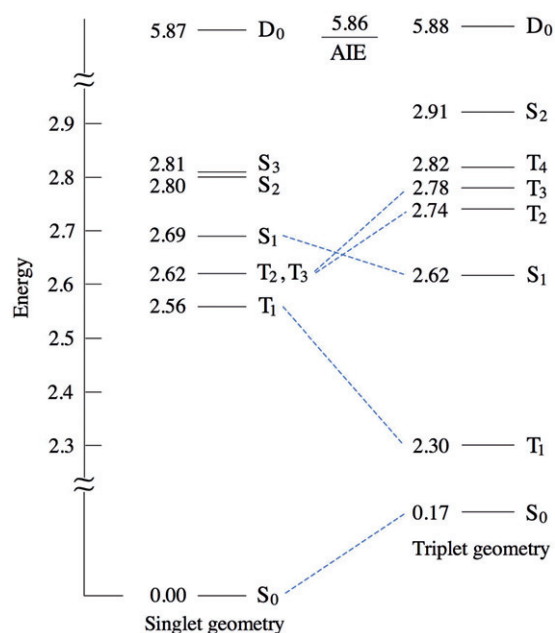


Figure 7. The first six BNL excited states at S_0 and T_1 geometries (in eV). Note that the adiabatic ionization energy (AIE) is 5.86 eV.

the experimental spectrum has been assigned to singlet-triplet transitions [15], where it is understood that the ‘triplets’ contain modest amounts of singlet character. The shoulder at 2.56 eV in the experimental spectrum is the same as our T_1 value (Table 6). Note that T_2 and T_3 , though close in energy to T_1 at the S_0 equilibrium geometry, are much higher in energy than T_1 at the T_1 equilibrium geometry (Figure 7).

The two intense bands at energies higher than 4 eV have been assigned to ligand-centred transitions ($^1LC \leftarrow S_0$). The broad absorbance below 4 eV is due primarily to spin-allowed transitions that terminate on metal-to-ligand charge transfer states (1MLCT). The shoulder at 2.56 eV in the experimental spectrum is attributed to 3MLCT by analogy with organic compounds. These assignments are qualitative because configuration interaction and spin-orbit coupling result in mixed state character [13].

The label MLCT is correct in the sense that metal-to-ligand electron transfer dominates. However, orbital analyses show that, in addition, a significant amount of charge is transferred from the phenyl to the pyridyl groups. Intra-ligand charge transfer also participates in ligand-centered transitions that involve asymmetric orbitals, *e.g.*, $\pi_{2a}^* \leftarrow d_{1a}$.

The BNL and experimental spectra are in agreement in terms of locations of maxima and overall shape. The $\omega B97X$ spectrum (Figure 6, inset) is

blue-shifted by almost 1 eV, and relative intensities of the three major bands match the experimental spectrum significantly less well. It is clearly of inferior quality and will not be considered further insofar as excited states are concerned. In assigning line shapes, the same FWHM (0.43 eV) was used for each transition. The high density of electronic states gives rise to broad bands. Because of the delocalized nature of the orbitals involved in the transitions, it is expected that the Franck–Condon factors are near diagonal, *i.e.* $\Delta v_i = 0$. Thus, transitions were taken as vertical from the S_0 equilibrium geometry, *i.e.* the nuclear degrees of freedom are treated classically. It would be unreasonable to expect a better match between experiment and theory.

At the T_1 equilibrium geometry, the 10 lowest singlets and 10 lowest triplets were calculated. Figure 7 and Tables 6 and 7 compare energies of excited states at the S_0 and T_1 equilibrium geometries. There are significant changes in the excited states between the S_0 and T_1 equilibrium geometries. For example, singlet and triplet potential surfaces cross (Figure 7).

3.4. Phosphorescence from T_1

Phosphorescence originates from T_1 vibrational levels, and in condensed phases it is assumed that vibrational relaxation takes place rapidly on the phosphorescence timescale. In other words, it is assumed, and rightly so, that the T_1 vibrational level populations are in thermal equilibrium during phosphorescence. Though the lowest frequency $\text{Ir}(\text{ppy})_3$ vibrational modes most likely couple well to the host, the picture of intramolecular vibrations remains nonetheless useful.

According to our calculations, at its equilibrium geometry the electronic energy of T_1 is 0.44 eV less than that of the next highest triplet, T_2 , whose energy is 0.04 eV below that of T_3 and 0.08 eV below that of T_4 . From the right hand column in Figure 7, one might consider subtracting 0.17 eV from 2.30 eV to obtain a $T_1 \rightarrow S_0$ emission origin of 2.13 eV. However, Yersin and coworkers have demonstrated, through detailed experimental studies carried out at temperatures as low as 1.5 K and with external magnetic fields as high as 12 Tesla, that the energy of the $T_1 \rightarrow S_0$ origin is 2.44 eV, and that this value depends little on the detailed nature of the host material [15].

Of course, the calculations do not include zero-point energy whereas the experiments do. More importantly, it is not the case that a calculation of the vertical electronic energy difference at the T_1 equilibrium geometry corresponds to the phosphorescence origin. The $\text{Ir}(\text{ppy})_3$ molecule has 177 vibrational

degrees of freedom, so an even-handed apportionment of 0.17 eV over these degrees of freedom results in each oscillator acquiring, on average, only 7.7 cm^{-1} . Also, if one calculates the average magnitude of the differences between the S_0 and T_1 equilibrium bond lengths listed in Table 1, this yields just 0.018 \AA . Moreover, of the 21 bond lengths listed in Table 1, three of the differences are a bit larger than the rest: Ir–C₄₉, C₄₈–C₄₉, and C₄₇–C₄₈. For the remaining 18, the average magnitude of the difference between the S_0 and T_1 equilibrium bond lengths is only 0.0088 \AA . Thus, most of the bond lengths differ little in going between S_0 and T_1 equilibrium geometries.

The picture this presents is one in which Franck–Condon factors for transitions that originate from the T_1 zero-point level are dominated by (0,0) contributions. Thus, the origin observed by Yersin and coworkers corresponds to our calculation of the energy of T_1 at its equilibrium geometry (2.30 eV) minus the energy of S_0 at its equilibrium geometry (0.00 eV). This agrees with the experimental value of 2.44 eV. Again, the calculations do not include vibrational zero-point energy nor do they include spin-orbit interaction, which results in additional shifts [10]. Note that the zero-field splitting of the three T_1 sublevels examined by Yersin and coworkers are minuscule on the energy scale of Figure 8, e.g. 19,693, 19,712, and 19,863 cm^{-1} in dichloromethane [15]. It is concluded that the theoretical and experimental values of the phosphorescence origin are in quite reasonable agreement.

3.5. Vibrational energy distribution

As mentioned earlier, at 500 K a significant amount of energy is present in the 177 vibrational degrees of freedom of ground electronic state gas phase Ir(ppy)₃. This energy is of course above and beyond the zero-point energy. The probability density for this ‘thermal’ vibrational energy, E_{vib} , shall be referred to as $P(E_{vib})$. The molecule’s rotational energy, whose average value at 500 K is 520 cm^{-1} , shall be left aside. It is modest relative to E_{vib} , and for the most part it is unavailable in gas phase intramolecular processes because of angular momentum conservation.

In addition, radiationless decay transforms ^1LC electronic excitation to T_1 electronic excitation, with mere vestiges of ^1LC and $^1\text{MLCT}$ electronic character distributed throughout the T_1 vibronic levels. Thus, the amount of vibrational energy imparted to T_1 via $^1\text{LC} \leftarrow S_0$ photoexcitation is approximately equal to $h\nu - E_{T_1}$ (see Figure 8), where E_{T_1} is the T_1 electronic energy. This energy is taken to be approximately

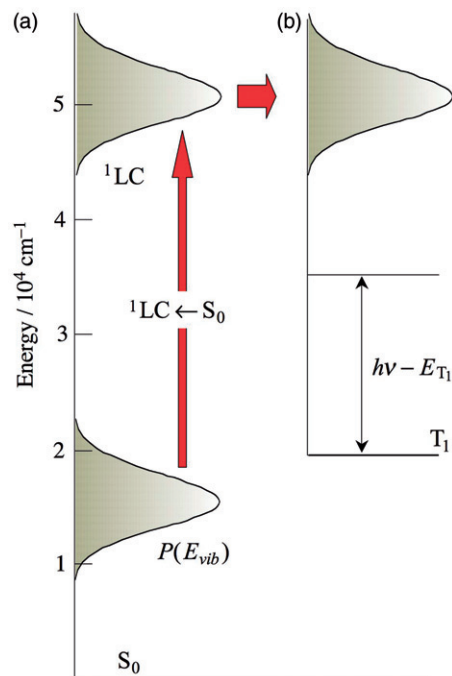


Figure 8. (a) Photoexcitation transports populated S_0 vibrational levels to ^1LC , which undergoes radiationless decay on a subpicosecond timescale, resulting ultimately in T_1 electronic excitation. This maps $P(E_{vib})$ to T_1 with additional T_1 vibrational energy given by $h\nu - E_{T_1}$, as indicated in (b) and in Figure 9.

$19,700\text{ cm}^{-1}$, as the sublevel energies are 19,693, 19,712, and $19,863\text{ cm}^{-1}$ in dichloromethane [15].

Adding $h\nu - E_{T_1}$ to the vibrational energy due to 500 K thermal equilibrium, E_{vib} , gives the total amount of T_1 vibrational energy. Once again, it is assumed that this is transformed essentially intact to vibrational excitation of the Ir(ppy)₃⁺ cation. However, whereas $h\nu - E_{T_1}$ is simply a number, the vibrational energy due to 500 K thermal equilibrium is distributed according to $P(E_{vib})$, and it is important to have at least a qualitative picture of how $P(E_{vib})$ varies with E_{vib} . For example, this variation gives the spread of vibrational energies carried over to the cation.

The main idea is illustrated schematically in Figure 8. Figure 8(a) indicates how $^1\text{LC} \leftarrow S_0$ photoexcitation transfers vibrational energy from S_0 to ^1LC , which in turn undergoes rapid radiationless decay (horizontal red arrow). In other words, a given S_0 molecule has a probability density $P(E_{vib})$ for being found in a small energy range centered at E_{vib} . Therefore photoexcitation maps $P(E_{vib})$ to essentially the same probability density in ^1LC , which in turn transfers it to T_1 , as indicated in Figure 8.

Pursuant to the above, a calculation of the 177 normal mode frequencies of Ir(ppy)₃ was carried out

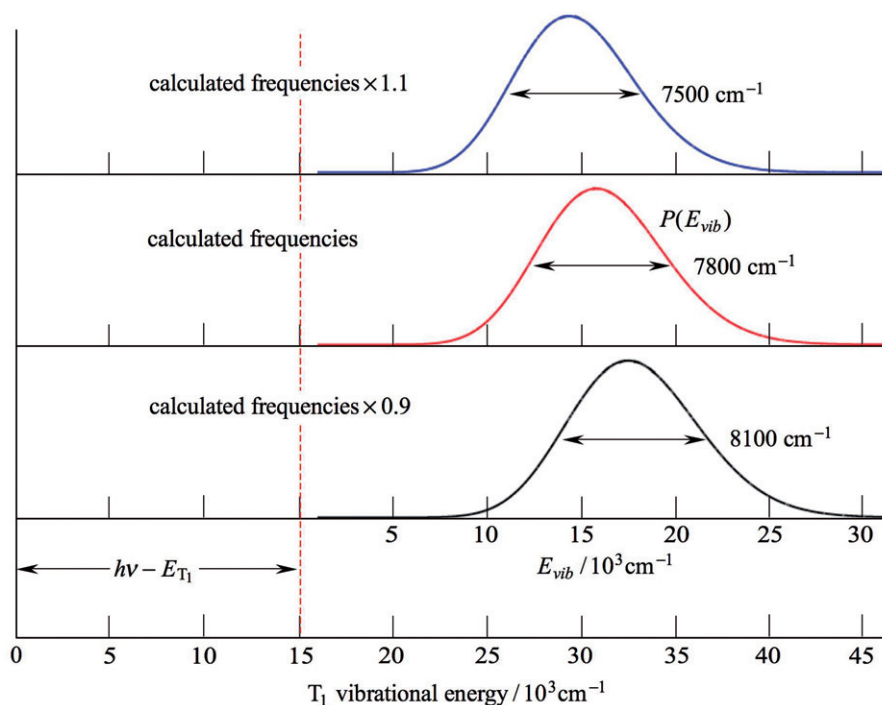


Figure 9. The red curve is a plot of Equation (2) with $T = 500$ K; see text for details. Following photoexcitation, the total vibrational energy in T_1 is given by $h\nu - E_{T_1} + E_{vib}$. The probability density for E_{vib} is $P(E_{vib})$, and $h\nu - E_{T_1} = 15,000$ cm^{-1} is chosen as a representative value. When all frequencies are changed by $\pm 10\%$, the $P(E_{vib})$ plots change accordingly (blue and black curves). However, the main qualitative feature is preserved. Namely, a considerable amount of T_1 vibrational energy is distributed with a FWHM that is modest relative to the energy of maximum $P(E_{vib})$, e.g. 7800 versus 31,000 cm^{-1} , respectively, for the red curve.

using B3LYP with lan12dz and 6-31+G* at the optimized geometry. The level of electronic structure theory used in this calculation is adequate, as the goal is a qualitative understanding of the shape of $P(E_{vib})$ versus E_{vib} . It is worth noting that $P(E_{vib})$ is not a strong function of vibrational frequency values, as discussed below and illustrated in Figure 9.

Carrying out calculations at the S_0 equilibrium geometry given in Table 1 resulted in five small-curvature saddle points, which are likely to be artifacts of numerical integration on a grid. When calculating density of states, the imaginary frequencies associated with these saddle points were replaced *ad hoc* with real frequencies of the same magnitudes: 45.7, 45.5, 31.6, 15.6, and 12.7 cm^{-1} . As long as these frequencies are significantly smaller than kT , the calculated $P(E_{vib})$ probability density is insensitive to their values. For example, increasing or decreasing these five frequencies by a factor of two causes the shapes of curves such as those in Figure 9 to change by no more than the thickness of the traces. Likewise, horizontal displacements are small, e.g. decreasing these five frequencies by a factor of two shifts the peak by +25 cm^{-1} , which

is minuscule on the scale of Figure 9. All of the frequencies are given in the SM.

With the vibrational frequencies in hand, the vibrational density of states $\rho(E_{vib})$ was calculated by using the MultiWell Program Suite, specifically, the Densum program, which employs the Beyer–Swinehart algorithm for harmonic oscillators [34–37]. This $\rho(E_{vib})$ was then multiplied by $e^{-E_{vib}/kT}$ (with $T = 500$ K) to obtain $P(E_{vib})$:

$$P(E_{vib}) = Z^{-1} \rho(E_{vib}) e^{-E_{vib}/kT} \quad (2)$$

where Z is the partition function. Plots of $P(E_{vib})$ are given in Figure 9.

Figure 9 illustrates the fact that altering the frequencies by a modest amount has a modest affect on the total T_1 vibrational energy. Specifically, combining $P(E_{vib})$ and $h\nu - E_{T_1}$ gives the probability density for vibrational energy within T_1 following $^1\text{LC} \leftarrow S_0$ photoexcitation (Figure 8). Referring to Figure 9, for an assumed value of $h\nu - E_{T_1} = 15,000$ cm^{-1} , the total T_1 vibrational energy peaks at $\sim 31,000$ cm^{-1} with a FWHM of ~ 7800 cm^{-1} . From the plots in Figure 9, it follows that the main

(qualitative) result would not change were a higher level of theory enlisted.

On the one hand, the use of a 500 K sample results in vibrational energy that we would rather were not present. On the other hand, the amount of vibrational energy imparted via photoexcitation is considerable and inevitable in experiments with gaseous $\text{Ir}(\text{ppy})_3$.

4. Summary

Electronic structure theory has been used to examine a number of excited singlet and triplet states of $\text{Ir}(\text{ppy})_3$ and a few low-lying states of $\text{Ir}(\text{ppy})_3^+$. Specifically, time-dependent density functional theory (TDDFT) calculations were carried out using long-range-corrected (LRC) ωB97X and BNL functionals. There is good agreement with several previous experimental and theoretical results [9–15,17], as well as with the experimental results presented in Paper I. The main conclusions are listed below.

- Yersin and coworkers have carried out detailed experimental studies of $T_1 \rightarrow S_0$ phosphorescence [15]. They report a 2.44 eV electronic origin and phosphorescence lifetimes of 0.2, 6.4, and 116 μs for the T_1 sublevels in dichloromethane [15]. The present calculations yield 2.30 eV, in agreement with the 2.44 eV experimental value. It was pointed out in Paper I that just a few percent of $^1\text{LC}/^1\text{MLCT}$ character is sufficient to reconcile the short phosphorescence lifetime of 0.2 μs because of the large oscillator strengths of the singlet–singlet transitions: $^1\text{LC} \leftarrow S_0$ and $^1\text{MLCT} \leftarrow S_0$. This degree of singlet–triplet mixing is in qualitative agreement with calculations of Nozaki that include SOC [13].
- The $^1\text{LC} \leftarrow S_0$ transition is accompanied by rapid radiationless decay of ^1LC , resulting ultimately in population of the phosphorescent state, T_1 . The number of electronically excited states having energy less than or equal to the photon energy is larger than the trio of states (^1LC , $^1\text{MLCT}$, and T_1) used in phenomenological models aimed at reconciling experimental results. In addition, potential surfaces cross, e.g. as seen in going between the S_0 and T_1 equilibrium geometries (Figure 7).
- A calculation of the ultraviolet absorption spectrum was carried out using 130 excited singlets obtained with the BNL functional. Oscillator strengths were calculated for

vertical excitation from the S_0 equilibrium geometry. The resulting stick spectrum was assigned a Gaussian shape with FWHM of 3470 cm^{-1} (0.43 eV) for each transition. This calculated spectrum is in agreement with the experimental room temperature absorption spectrum. This agreement is consistent with Franck–Condon factors dominated by $\Delta v_i = 0$, as expected for the delocalized nature of the orbitals involved.

- The calculated adiabatic and vertical (S_0 and T_1 equilibrium geometries) ionization energies are 5.86, 5.87, and 5.88 eV, respectively. These values agree with the calculated result of 5.94 eV reported by Hay [10], as well as with the conservative experimental upper bound of 6.4 eV reported in Paper I. It is concluded that the ionization energy is in the vicinity of 6 eV. This low ionization energy is advantageous for OLED applications.
- The probability density for finding a gas phase $\text{Ir}(\text{ppy})_3$ molecule with ‘thermal’ vibrational energy E_{vib} at temperature T is: $P(E_{vib}) = Z^{-1} \rho(E_{vib}) \exp(-E_{vib}/kT)$, where Z is the partition function. This can be combined with the vibrational energy imparted through photoexcitation, $h\nu - E_{T_1}$, to obtain the probability density as a function of total vibrational energy. In rough terms, for 500 K this probability density peaks at $\sim 31,000\text{ cm}^{-1}$ (3.84 eV) with a FWHM spread of $\sim 7800\text{ cm}^{-1}$ (0.97 eV) (Figure 9). It is interesting that, despite this large amount of vibrational energy, 2-photon ionization is dominated by the parent cation $\text{Ir}(\text{ppy})_3^+$, with no discernible fragmentation over a significant frequency range [8].
- Qualitative understanding of the photophysics of this system is assisted greatly by the MO’s obtained at the S_0 , T_1 , and D_0 equilibrium geometries.

Acknowledgements

The authors are pleased to acknowledge the valuable assistance of Dr Yihan Shao from QChem, Inc. This research has been supported through grants from the National Science Foundation. The experimental work was supported by CHE-0652830 (CN, JF, ZL, and CW). The theoretical work was conducted under the auspices of the iOpenShell Center for Computational Studies of Electronic Structure and Spectroscopy of Open-Shell and Electronically Excited Species: CRIF:CRF CHE-0625419-0624602-0625237 and CHE-0951634 (AIK and KD).

References

- [1] H. Yersin (ed.), *Highly Efficient OLEDs with Phosphorescent Materials* (Wiley-VCH Verlag GmbH & Co., Weinheim, 2008).
- [2] H. Yersin and W.J. Finkenzeller, in *Highly Efficient OLEDs with Phosphorescent Materials*, edited by H. Yersin (Wiley-VCH Verlag GmbH & Co., Weinheim, 2008), pp. 1–97.
- [3] H. Yersin, *Top. Curr. Chem.* **241**, 1 (2004).
- [4] A.F. Rausch, H.H.H. Homeier and H. Yersin, *Top. Organomet. Chem.* **29**, 193 (2010).
- [5] H. Yersin, A.F. Rausch, R. Czerwieniec, T. Hofbeck and T. Fischer, *Coord. Chem. Rev.* **255**, 2622 (2011).
- [6] M.A. Baldo, M.E. Thompson and S.R. Forrest, *Nature* **403**, 750 (2000).
- [7] V. Cleave, G. Yahsioglu, P. Le Barny, R.H. Friend and N. Tessler, *Adv. Mater.* **11**, 285 (1999).
- [8] C. Nemirow, J. Fine, Z. Lu, K. Diri, A.I. Krylov and C. Wittig, Photoionization of tris(2-phenylpyridine)iridium, accompanying (preceding) paper.
- [9] T. Matsushita, T. Asada and S. Koseki, *J. Phys. Chem. C* **111**, 6897 (2007).
- [10] P.J. Hay, *J. Phys. Chem. A* **106**, 1634 (2002).
- [11] E. Jansson, B. Minaev, S. Schrader and H. Ågren, *Chem. Phys.* **333**, 157 (2007).
- [12] X.D. Liu, J.K. Feng, A.M. Ren, L. Yang, B. Yang and Y.G. Ma, *Opt. Mater.* **29**, 231 (2006).
- [13] K. Nozaki, *J. Chinese Chem. Soc.* **53**, 101 (2006).
- [14] W.J. Finkenzeller and H. Yersin, *Chem. Phys. Lett.* **377**, 299 (2003).
- [15] T. Hofbeck and H. Yersin, *Inorg. Chem.* **49**, 9290 (2010).
- [16] A.V. Kukhta, I.N. Kukhta, S.A. Bagnich, S.M. Kazakov, V.A. Andreev, O.L. Neyra and E. Meza, *Chem. Phys. Lett.* **434**, 11 (2007).
- [17] A.B. Tamayo, B.D. Alleyne, P.I. Djurovich, S. Lamansky, I. Tsyba, N.N. Ho, R. Bau and M.E. Thompson, *J. Am. Chem. Soc.* **125**, 7377 (2003).
- [18] J.D. Chai and M. Head-Gordon, *J. Chem. Phys.* **128**, 084106 (2008).
- [19] J.D. Chai and M. Head-Gordon, *Phys. Chem. Chem. Phys.* **10**, 6615 (2008).
- [20] R. Baer and D. Neuhauser, *Phys. Rev. Lett.* **94**, 043002 (2005).
- [21] E. Livshits and R. Baer, *Phys. Chem. Chem. Phys.* **9**, 2932 (2007).
- [22] A. Lange and J.M. Herbert, *J. Chem. Theory Comput.* **3**, 1680 (2007).
- [23] P.J. Hay and W.R. Wadt, *J. Chem. Phys.* **82**, 299 (1985).
- [24] W.J. Hehre, R.F. Stewart and J.A. Pople, *J. Chem. Phys.* **51**, 2657 (1969).
- [25] R. Baer, E. Livshits and U. Salzner, *Ann. Rev. Phys. Chem.* **61**, 85 (2010).
- [26] QChem User's Manual, version 3.2 (2011).
- [27] Y. Shao, L.F. Molnar, Y. Jung, J. Kussmann, C. Ochsenfeld, S.T. Brown, A.T.B. Gilbert, L.V. Slipchenko, S.V. Levchenko, D.P. O'Neill, R.A. DiStasio, R.C. Lochan, T. Wang, G.J.O. Beran, N.A. Besley, J.M. Herbert, C.Y. Lin, T. Van Voorhis, S.H. Chien, A. Sodt, R.P. Steele, V.A. Rassolov, P.E. Maslen, P.P. Korambath, R.D. Adamson, B. Austin, J. Baker, E.F.C. Byrd, H. Dachsel, R.J. Doerksen, A. Dreuw, B.D. Dunietz, A.D. Dutoi, T.R. Furlani, S.R. Gwaltney, A. Heyden, S. Hirata, C.P. Hsu, G. Kedziora, R.Z. Khalliulin, P. Klunzinger, A.M. Lee, M.S. Lee, W. Liang, I. Lotan, N. Nair, B. Peters, E.I. Proynov, P.A. Pieniazek, Y.M. Rhee, J. Ritchie, E. Rosta, C.D. Sherrill, A.C. Simmonett, J.E. Subotnik, H.L. Woodcock, W. Zhang, A.T. Bell, A.K. Chakraborty, D.M. Chipman, F.J. Keil, A. Warshel, W.J. Hehre, H.F. Schaefer, J. Kong, A.I. Krylov, P.M.W. Gill and M. Head-Gordon, *Phys. Chem. Chem. Phys.* **8**, 3172 (2006).
- [28] F.H. Allen, O. Kennard, J.J. Galloy, O. Johnson and D.G. Watson, *Chem. Structures* **2**, 343 (1993).
- [29] J. Breu, P. Stossel, S. Schrader, A. Starukhin, W.J. Finkenzeller and H. Yersin, *Chem. Mater.* **17**, 1745 (2005).
- [30] F.O. Garces, K. Dedeian, N.L. Keder and R.J. Watts, *Acta Crystallogr. C* **49**, 1117 (1993).
- [31] B.J. Coe and S.J. Glenwright, *Coord. Chem. Rev.* **203**, 5 (2000).
- [32] F.R. Hartley, *Chem. Soc. Rev.* **2**, 163 (1973).
- [33] U. Salzner and R. Baer, *J. Chem. Phys.* **131**, 23110 (2009).
- [34] J.R. Barker, N.F. Ortiz, J.M. Preses, L.L. Lohr, A. Maranzana, P.J. Stimac, T.L. Nguyen and T.J. Dhilip Kumar, MultiWell-2011.3 Software, <http://aos-s.engin.umich.edu/multiwell>
- [35] T. Beyer and D. Swinehart, *Comm. ACM* **16**, 379 (1973).
- [36] J.R. Barker, *Int. J. Chem. Kin.* **33**, 232 (2001).
- [37] J.R. Barker, *Int. J. Chem. Kin.* **41**, 748 (2009).